Topologically Protected Quantum Metallic Bonding of Alkali Metals

from Entangled Electron-Phonon Dynamics Supplementary Materials

Hang Hu[1)], Hsu Kiang Ooi[2)], Mohammad S. Ghaemi[2)] Junan Lin[2)] Jiří Hostaš[1)] and Anguang Hu[3*)]

[1)]Digital Technologies Research Center, Digital Technologies, National Research Council of Canada, 2107 chemin de la Polytechnique Montréal, QC H3T 1J4, Canada

[2)]Digital Technologies Research Center, Digital Technologies, National Research Council of Canada, 222 College Street, Toronto, M5T 3J1, ON, Canada

[3)] Suffield Research Centre, Defence Research and Development Canada, PO Box 4000 Station Main, Medicine Hat, Alberta, Canada, T1A 8K6

*Corresponding author. E-mail: Anguang.Hu@drdc-rddc.gc.ca

Lattice parameters for all the studied crystal structures are provided in Table S1. The calculated time evolution of dynamic energy change between the degeneracy-lifting electronic system and the phonon field in sodium (Na), potassium (K), rubidium (Rb), and cesium (Cs) is shown in Figure S1. Tables S2-S6 list calculated vibrational frequencies and normal mode coordinates of Li, Na, K, Rb and Cs, respectively.

Table S1. Calculated lattice parameters of alkali metals at ambient conditions

Atom	Space group	Lattice parameters (Å)
Li	$Im\bar{3}m$	a = 3.4273
Na	$Im\bar{3}m$	a = 4.2906
K	$Im\bar{3}m$	a = 5.2822
Rb	$Im\bar{3}m$	a = 5.6990
Cs	$Im\bar{3}m$	a = 6.1620

Table S2. Vibrational frequencies and corresponding normal mode coordinates of Li

Frequencies (cm^{-1})	Normal mode coordinates (Å)		
0.0	0.00000	-0.70711	0.00000
	0.00000	-0.70711	0.00000
0.0	-0.70711	0.00000	0.00000
	-0.70711	0.00000	0.00000
0.0	0.00000	0.00000	-0.70711
	0.00000	0.00000	-0.70711
310.40	0.00000	0.70711	0.00000
	0.00000	-0.70711	0.00000
310.40	0.00000	0.00000	-0.70711
	0.00000	0.00000	0.70711
310.40	-0.70711	0.00000	0.00000
	0.70711	0.00000	0.00000

Table S3. Vibrational frequencies and corresponding normal mode coordinates of Na

Frequencies (cm^{-1})	Normal mode coordinates (Å)		
0.0	0.00000	-0.70711	0.00000

	0.00000	-0.70711	0.00000
0.0	-0.70711	0.00000	0.00000
	-0.70711	0.00000	0.00000
0.0	0.00000	0.00000	-0.70711
	0.00000	0.00000	-0.70711
99.72	0.00000	0.70711	0.00000
	0.00000	-0.70711	0.00000
99.72	0.00000	0.00000	-0.70711
	0.00000	0.00000	0.70711
99.72	-0.70711	0.00000	0.00000
	0.70711	0.00000	0.00000

Table S4. Vibrational frequencies and corresponding normal mode coordinates of K

Frequencies (cm^{-1})	Normal mode coordinates (Å)		
0.0	0.00000	-0.70711	0.00000
	0.00000	-0.70711	0.00000
0.0	-0.70711	0.00000	0.00000
	-0.70711	0.00000	0.00000
0.0	0.00000	0.00000	-0.70711
	0.00000	0.00000	-0.70711
60.99	0.00000	0.70711	0.00000
	0.00000	-0.70711	0.00000
60.99	0.00000	0.00000	-0.70711
	0.00000	0.00000	0.70711
60.99	-0.70711	0.00000	0.00000
	0.70711	0.00000	0.00000

Table S5. Vibrational frequencies and corresponding normal mode coordinates of Rb

Frequencies (cm^{-1})	Normal mode coordinates (Å)		
0.0	0.00000	-0.70711	0.00000
	0.00000	-0.70711	0.00000
0.0	-0.70711	0.00000	0.00000
	-0.70711	0.00000	0.00000
0.0	0.00000	0.00000	-0.70711
	0.00000	0.00000	-0.70711
35.45	0.00000	0.70711	0.00000
	0.00000	-0.70711	0.00000
35.45	0.00000	0.00000	-0.70711
	0.00000	0.00000	0.70711
35.45	-0.70711	0.00000	0.00000
	0.70711	0.00000	0.00000

Table S6. Vibrational frequencies and corresponding normal mode coordinates of Cs

Frequencies (cm^{-1})	Normal mode coordinates (Å)		
0.0	0.00000	-0.70711	0.00000
	0.00000	-0.70711	0.00000
0.0	-0.70711	0.00000	0.00000
	-0.70711	0.00000	0.00000
0.0	0.00000	0.00000	-0.70711
	0.00000	0.00000	-0.70711
31.37	0.00000	0.70711	0.00000
	0.00000	-0.70711	0.00000
31.37	0.00000	0.00000	-0.70711
	0.00000	0.00000	0.70711
31.37	-0.70711	0.00000	0.00000
	0.70711	0.00000	0.00000

Finite-difference evaluation of band-energy derivatives.

Supplemental equations (1) and (2) are used to evaluate the first- and second-order derivatives of the electronic band energy ε_{nk} with respect to a vibrational-mode coordinate u_{qv} using a symmetric 5-point stencil with step Δu_{qv}:

$$\left.\frac{\partial \varepsilon_{nk}}{\partial u_{qv}}\right|_0 \approx \frac{-\varepsilon_{nk}(2\Delta u_{qv}) + 8\,\varepsilon_{nk}(\Delta u_{qv}) - 8\,\varepsilon_{nk}(-\Delta u_{qv}) + \varepsilon_{nk}(-2\Delta u_{qv})}{12\,\Delta u_{qv}} \tag{A1}$$

$$\left.\frac{\partial^2 \varepsilon_{nk}}{\partial u_{qv}^2}\right|_0 \approx \frac{-\varepsilon_{nk}(2\Delta u_{qv}) + 16\,\varepsilon_{nk}(\Delta u_{qv}) - 30\,\varepsilon_{nk}(0) + 16\,\varepsilon_{nk}(-\Delta u_{qv}) - \varepsilon_{nk}(-2\Delta u_{qv})}{12\,(\Delta u_{qv})^2} \tag{A2}$$

While Eqs. (A1)-(A2) provide a numerical route to the derivatives, we verified their accuracy by checking that the first-order derivative of band energies with respect to u_{qv} vanishes at the equilibrium structure throughout the Brillouin zone; in our calculations, all first-order derivatives are zero within 0.1 meV/Å.

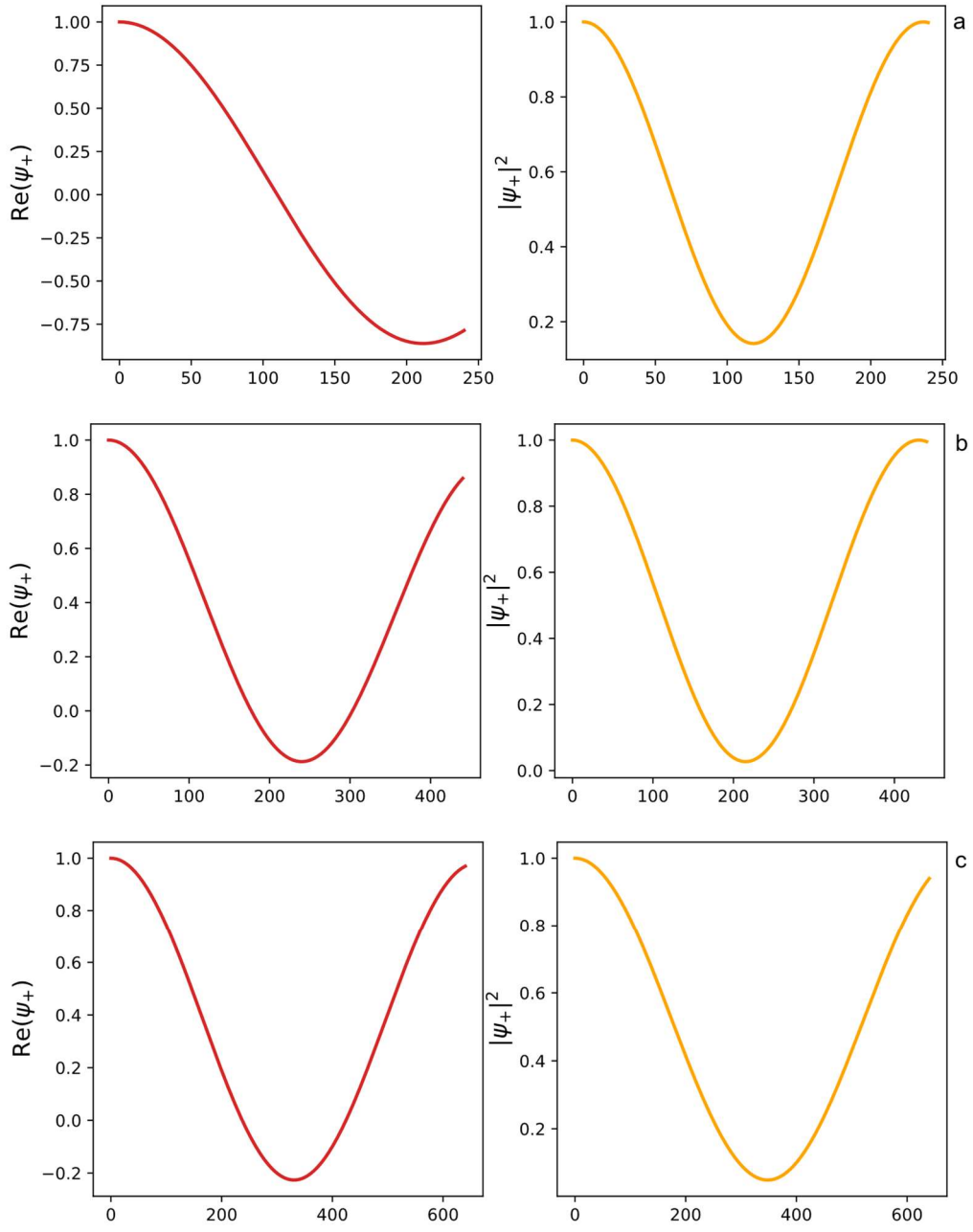

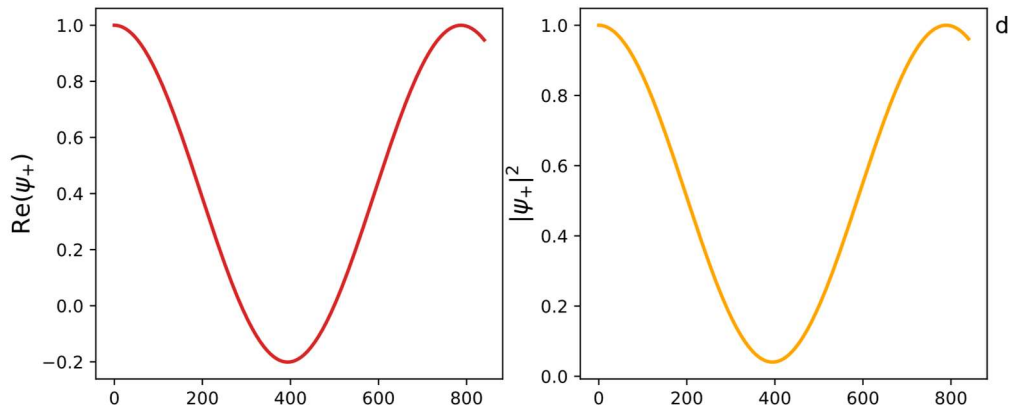

Figure S1. Time evolution of the real part (left) and probability amplitude squared (right) of the |+⟩ state in a two-level system driven by a static perturbation for Na (a), K (b), Rb (c) and Cs (d). The dynamics illustrate coherent oscillation and population transfer governed by the system's intrinsic Hamiltonian parameters.

In our study, we specifically analyze the second optical phonon mode for all the alkali elements. The mode coordinates are listed in Table S2, S3, S4, S5, and S6. Electron–phonon coupling arises from modulations of the electronic potential, which are most effectively generated by longitudinal vibrations (shown in red in Table S2-26), where atomic displacements are aligned with the phonon propagation vector. Transverse or mixed-polarized modes typically produce modulations that couple weakly to electronic states without the equal and opposite peaks, as shown in Figures S2, S3, S4, S5, S6 for Li, Na, K, Rb, Cs. In contrast, the Γ-point longitudinal mode generates a large antisymmetric potential modulation, consistent with a dynamic Jahn–Teller–like mechanism. This selective symmetry breaking directly impacts the degenerate bands at the Fermi surface. Additionally, our mode-resolved calculations across the phonons at other q vectors, such as A, P, N, and H, also exhibit only weak coupling to the nearly degenerate bands at the Fermi level, as shown in Figures S7, S8, S9 and S10. Some of these phonon modes will exhibit equal and opposite peaks, but the intensity is much lower. For lithium, the general curvature pattern of Figure S7c, S8c, and S9a is similar to Figure 2a, but the peaks are ±60 eV/Å^2 for the mode at the Γ-point versus ±5 eV/Å^2 for the mode at the other q vectors. The Γ-point longitudinally polarized mode induces a pronounced band renormalization and clear degeneracy lifting, reflecting a much stronger interaction. This selectivity provides a natural criterion for focusing on the Γ mode as the dominant contributor and the focus of our study.

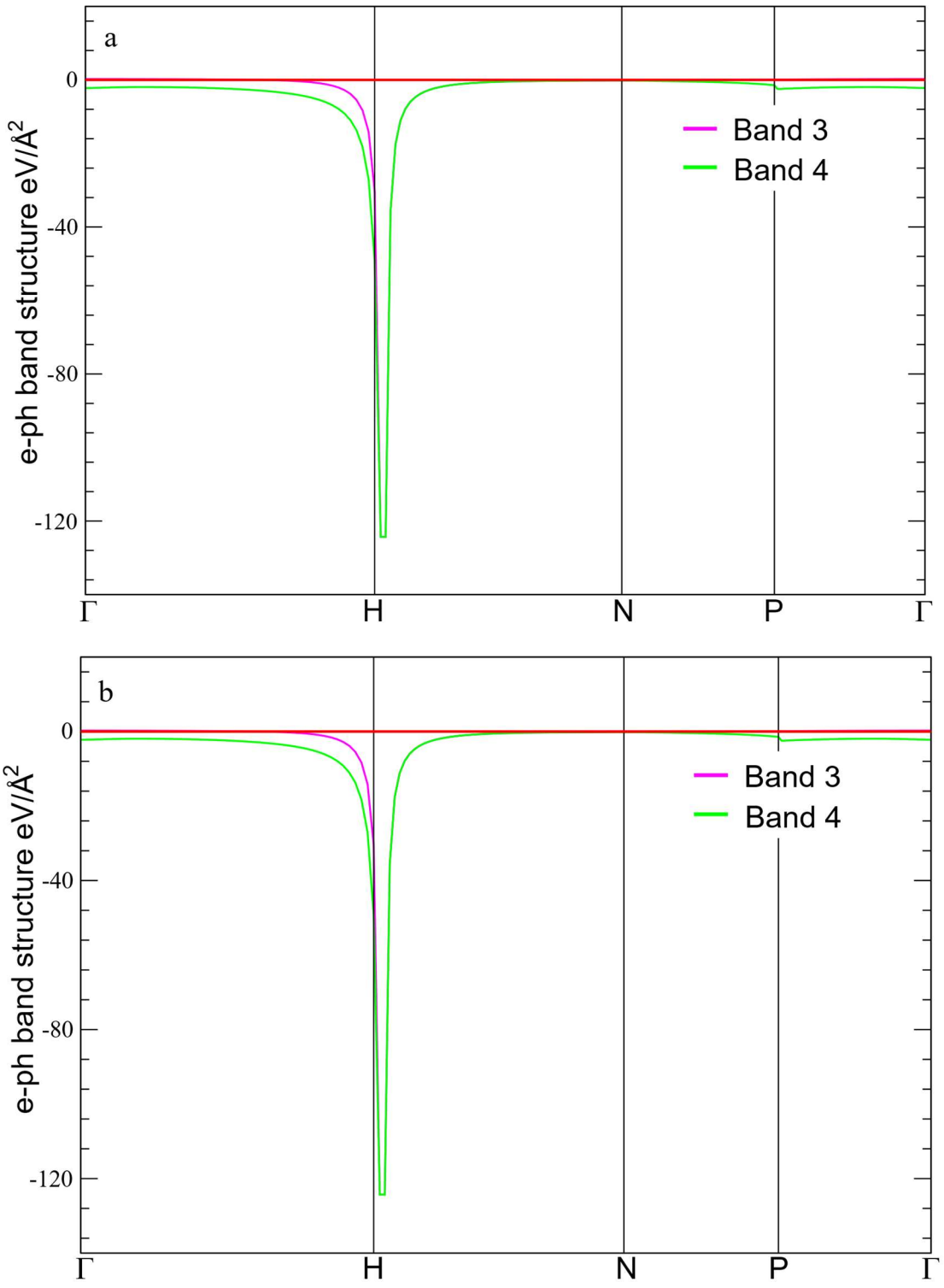

Figure S2. Mode-resolved electron–phonon band structures of Li's other two optical phonon modes, with vibration along the x-axis (a) and y-axis (b).

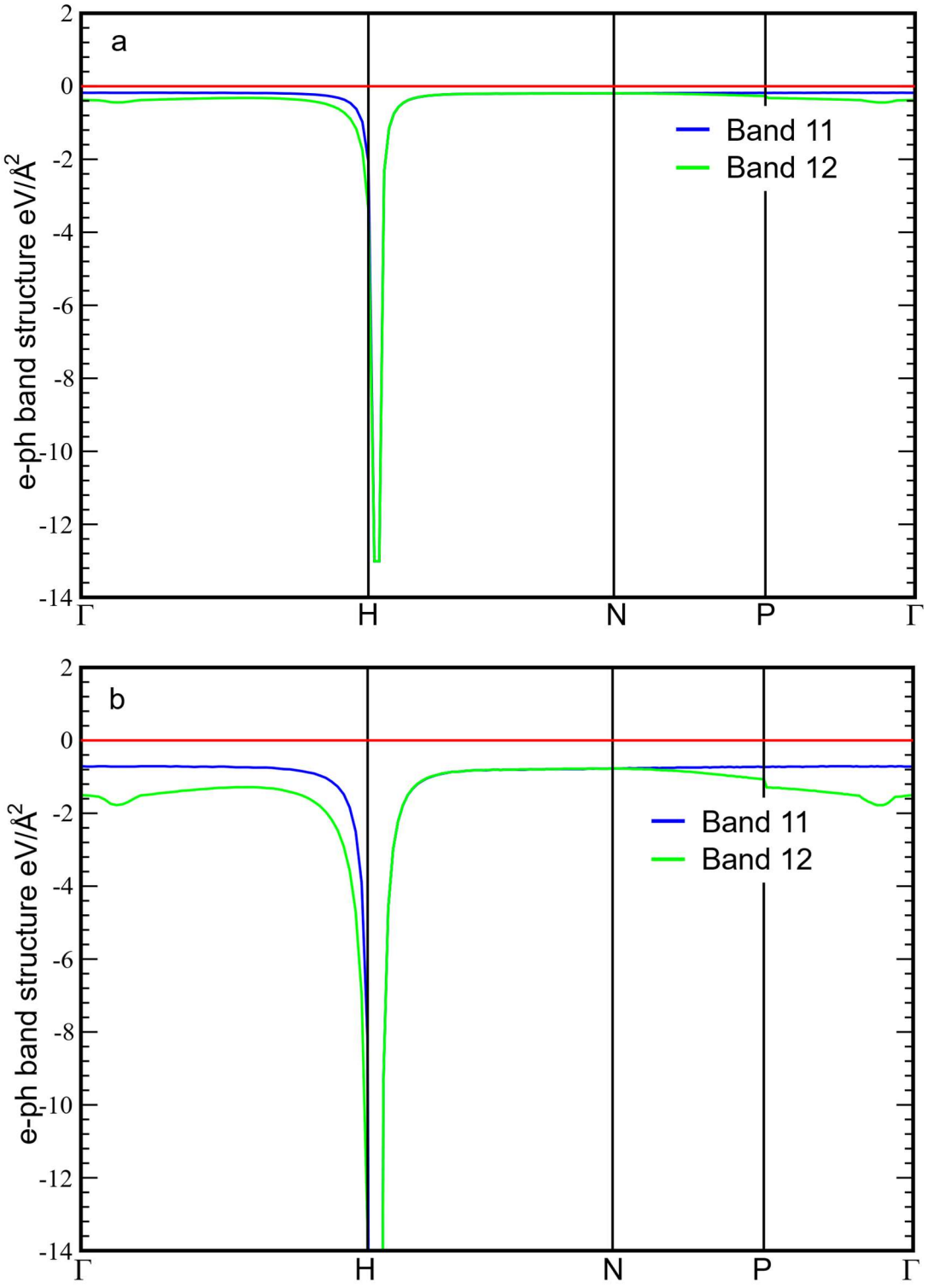

Figure S3. Mode-resolved electron–phonon band structures of Na's other two optical phonon modes, with vibration along the x-axis (a) and y-axis (b).

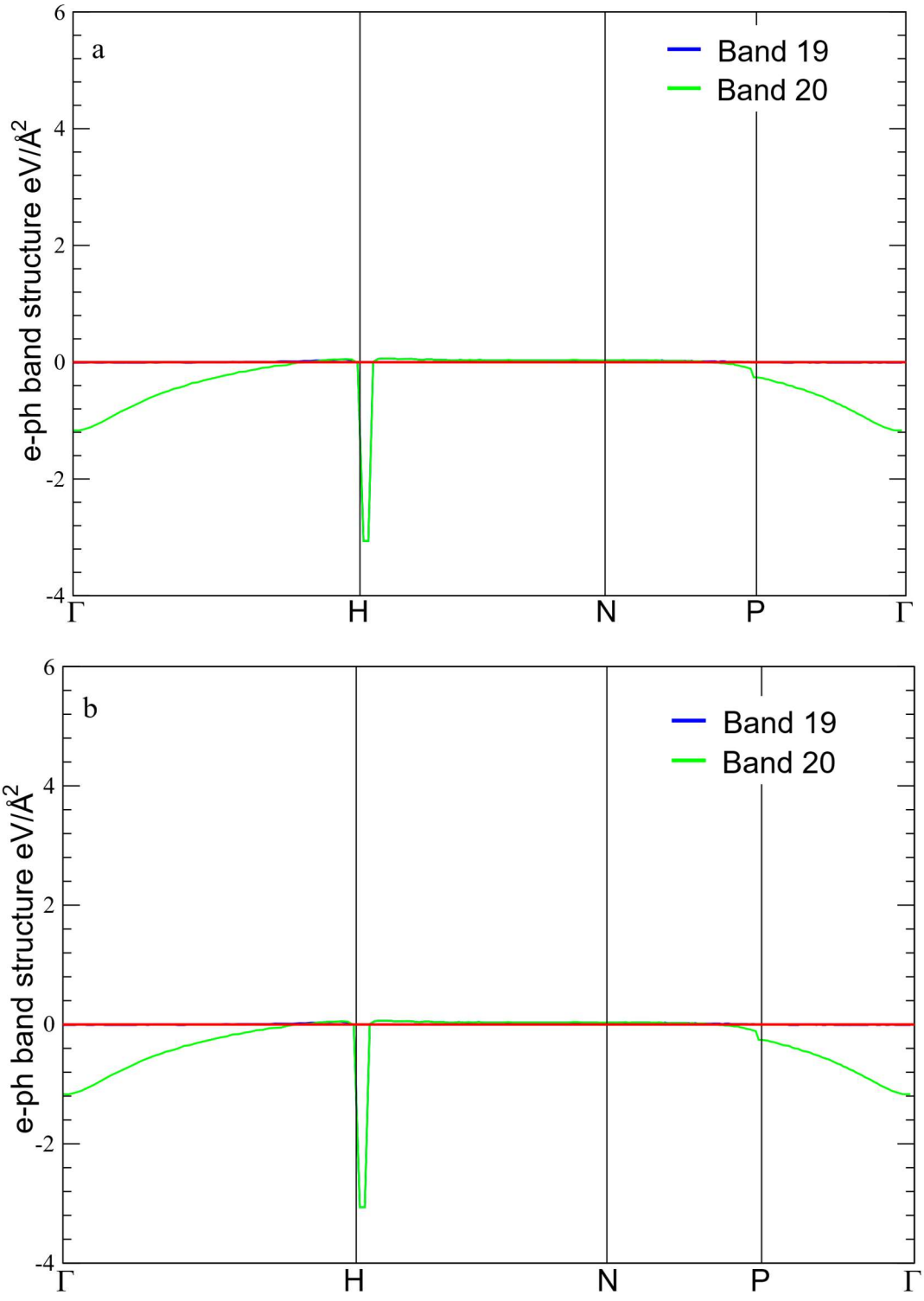

Figure S4. Mode-resolved electron–phonon band structures of K's other two optical phonon modes, with vibration along the x-axis (a) and y-axis (b).

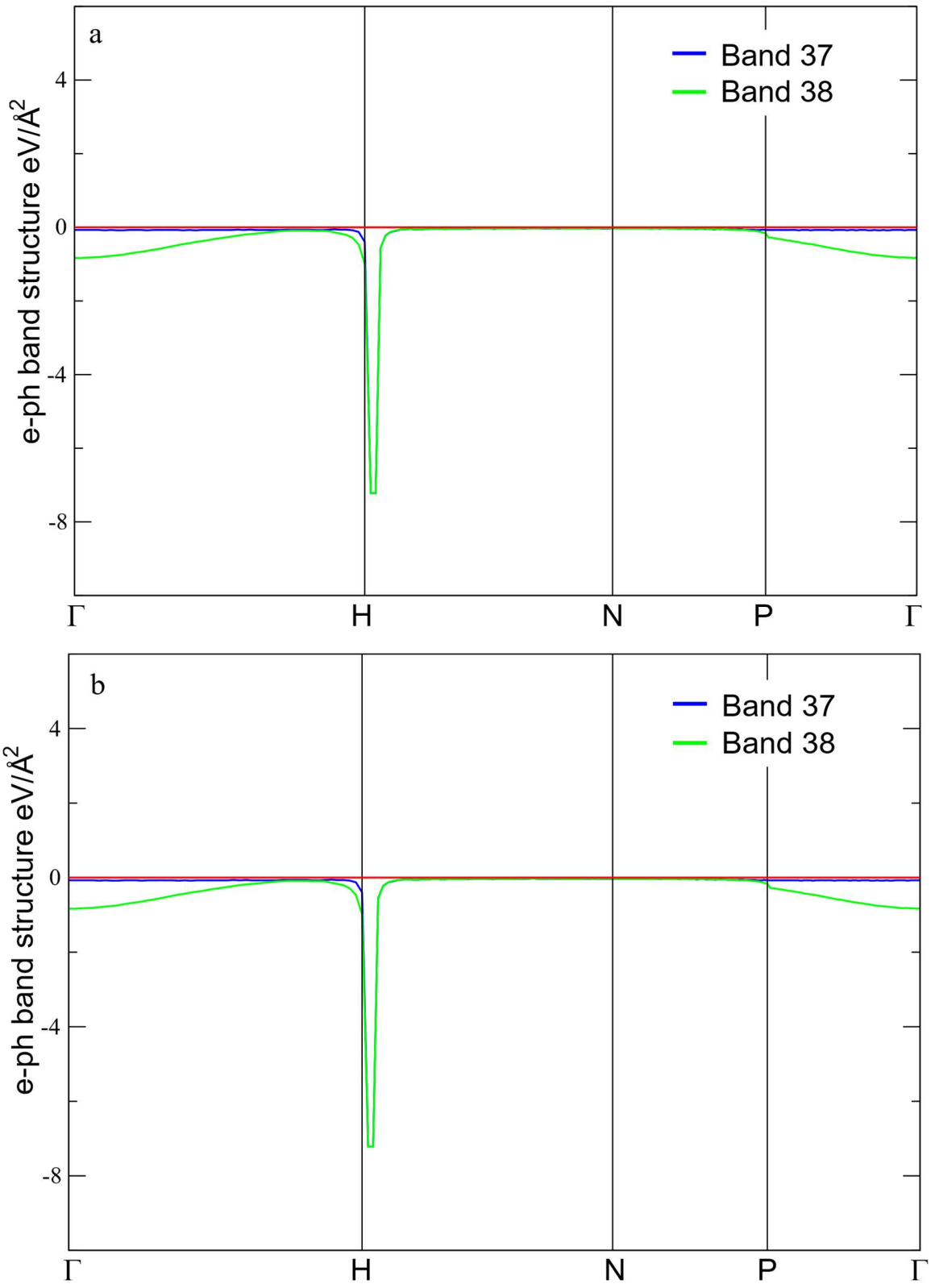

Figure S5. Mode-resolved electron–phonon band structures of Rb's other two optical phonon modes, with vibration along the x-axis (a) and y-axis (b).

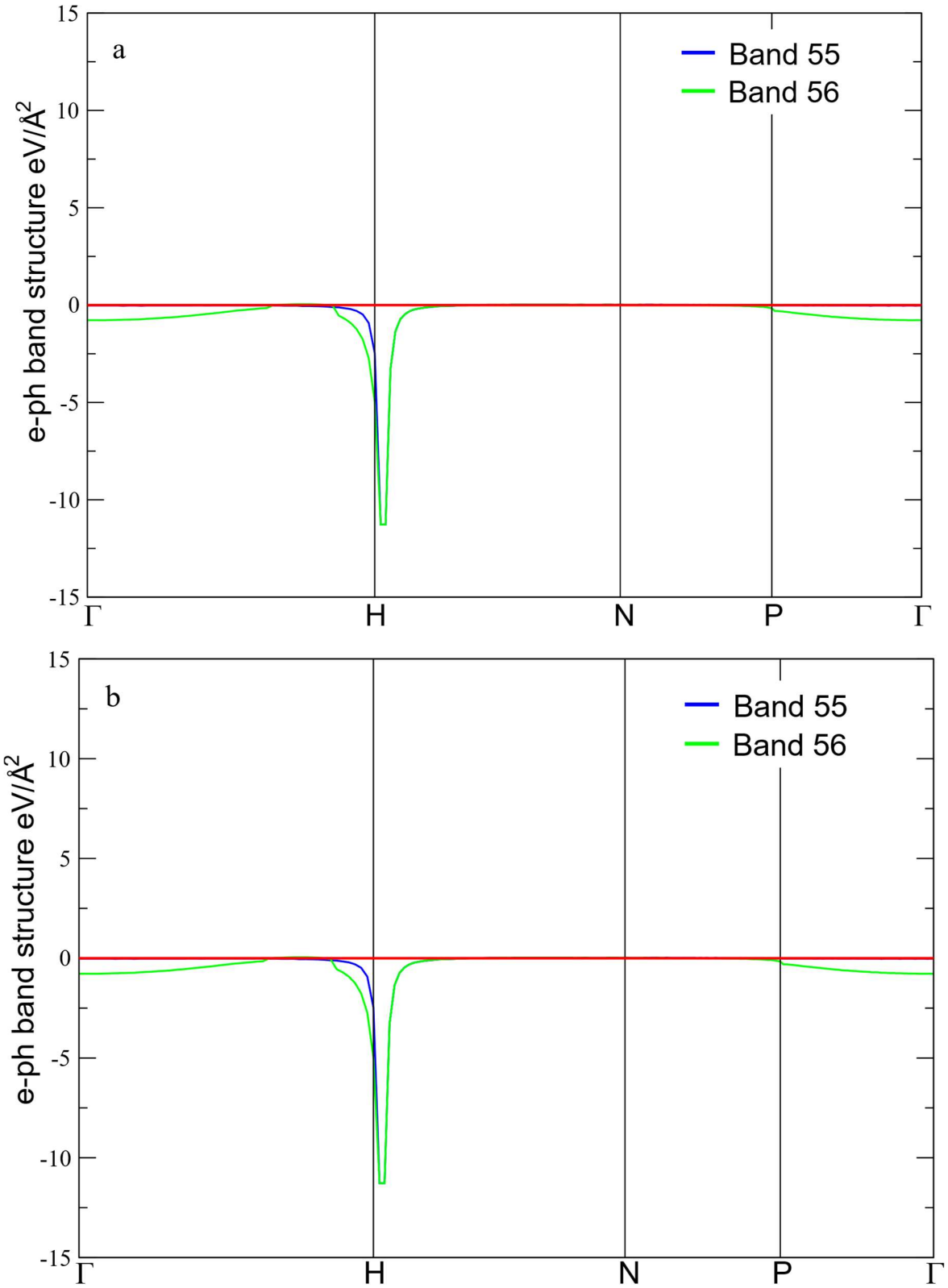

Figure S6. Mode-resolved electron–phonon band structures of Cs's other two optical phonon modes, with vibration along the x-axis (a) and y-axis (b).

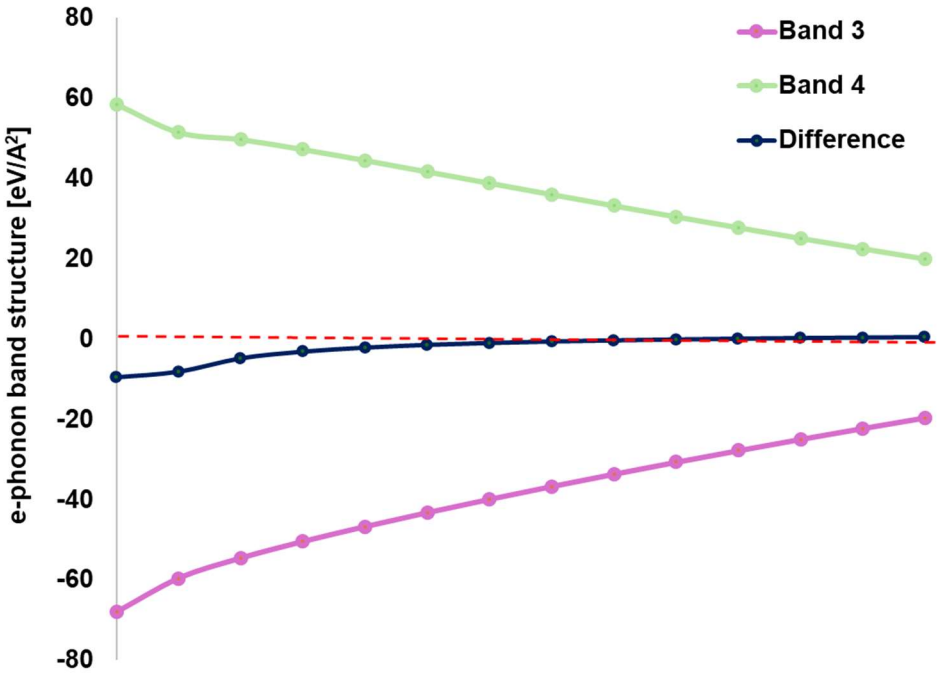

Figure S7. Zoom in on the H point longitudinal-mode, mode-resolved e–ph band structure of Li (Figure 2a). The partner bands (3 and 4) show a resonant, equal-and-opposite response at the BCC H point. The pairwise difference approaches zero within a few sampled k-points from H; the small residual at the first point lies just outside the isolated two-level (Dirac) window. Remaining offsets are within numerical noise from finite-window sampling.

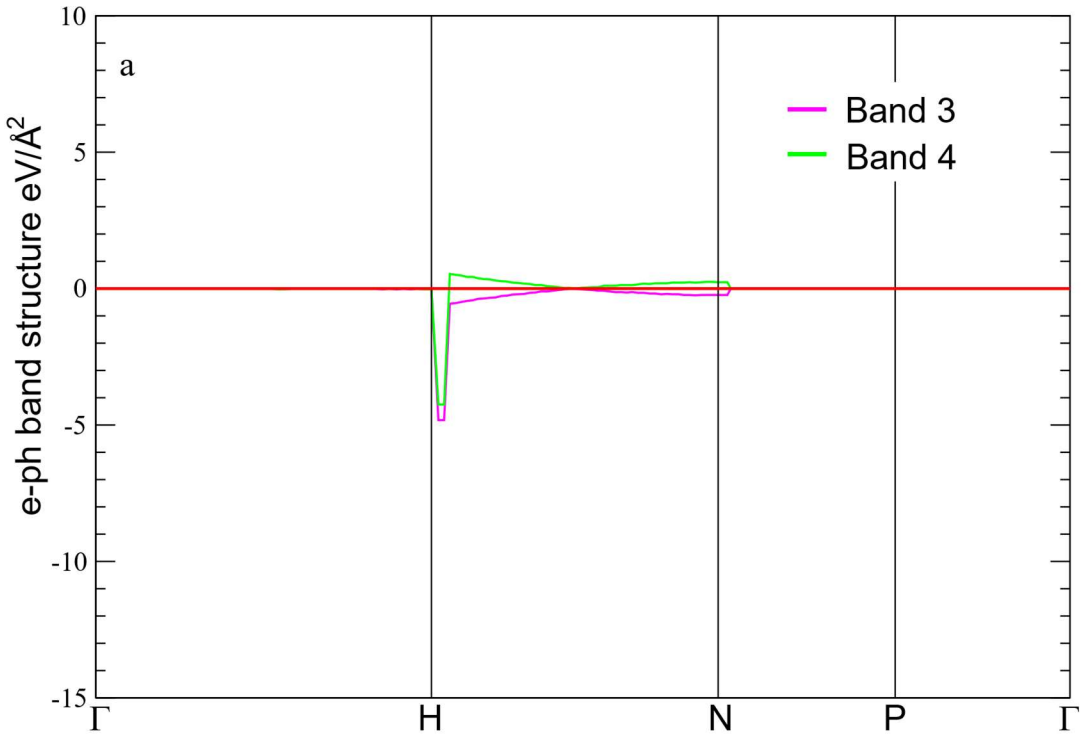
a
Band 3
Band 4
e-ph band structure eV/Å^2
10
5
0
-5
-10
-15
Γ
H
N
P
Γ

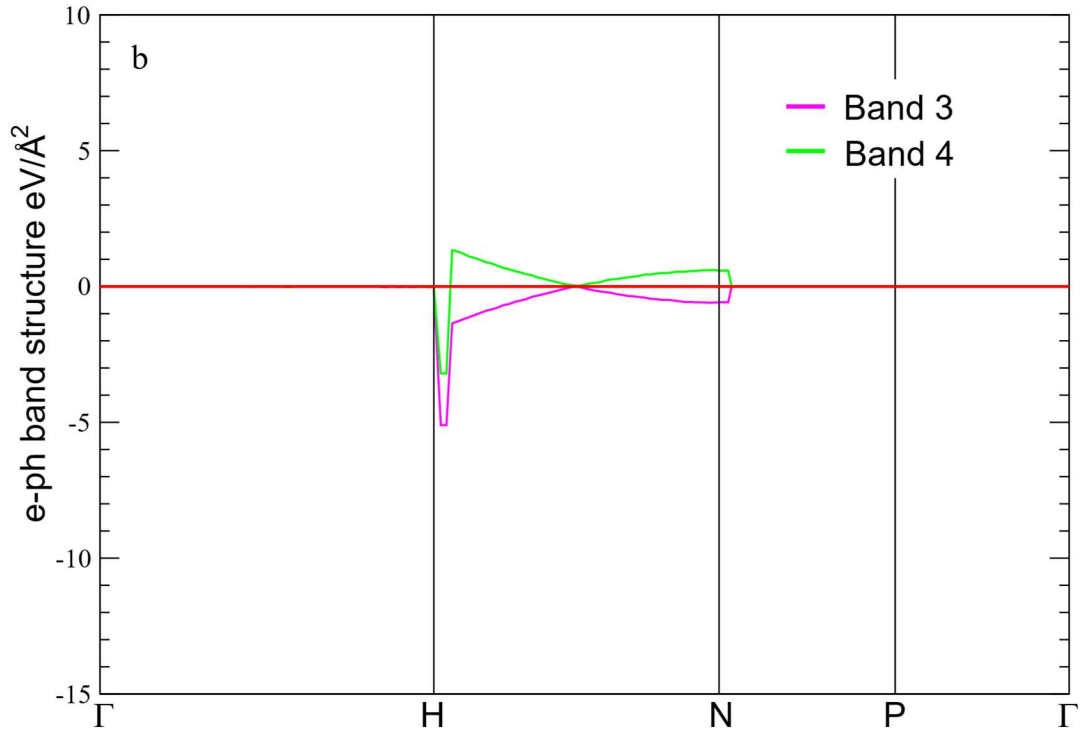
b
Band 3
Band 4
e-ph band structure eV/Å^2
10
5
0
-5
-10
-15
Γ
H
N
P
Γ

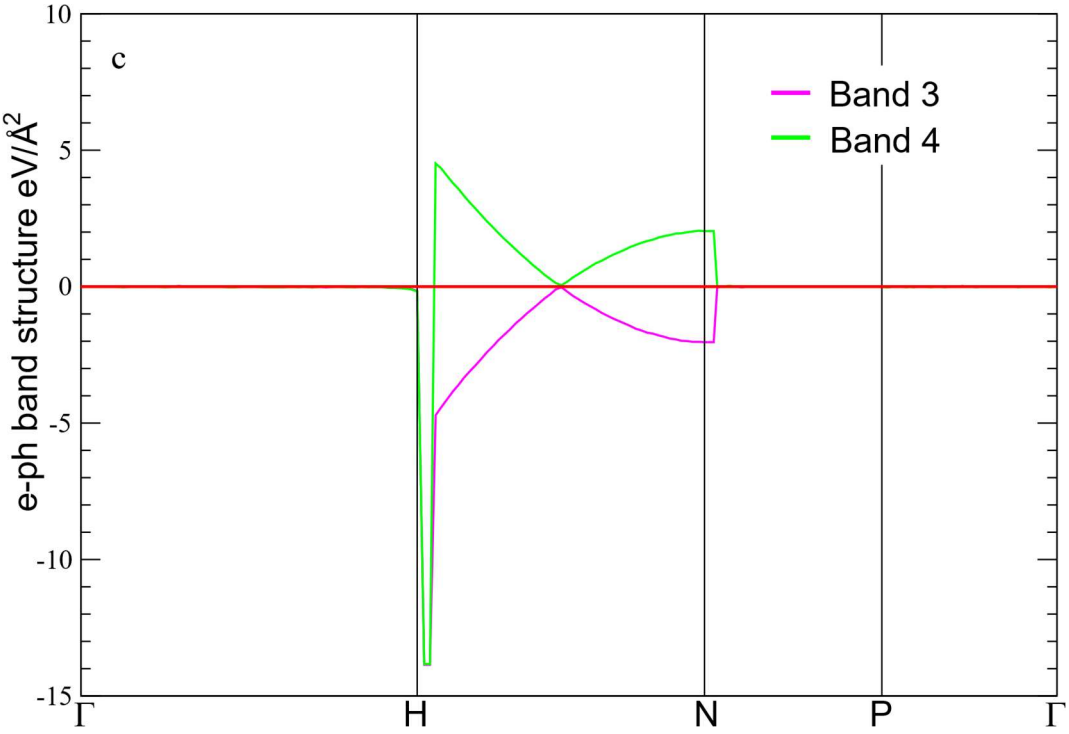

Figure S8. Mode-resolved electron–phonon band structures of lithium, characterized by the second-order derivatives of the band energies with respect to phonon displacements at the A point (q = 0.1, 0.5, 0.1) and plotted along high-symmetry paths in the Brillouin zone (e.g. Γ–H–N–P–Γ).

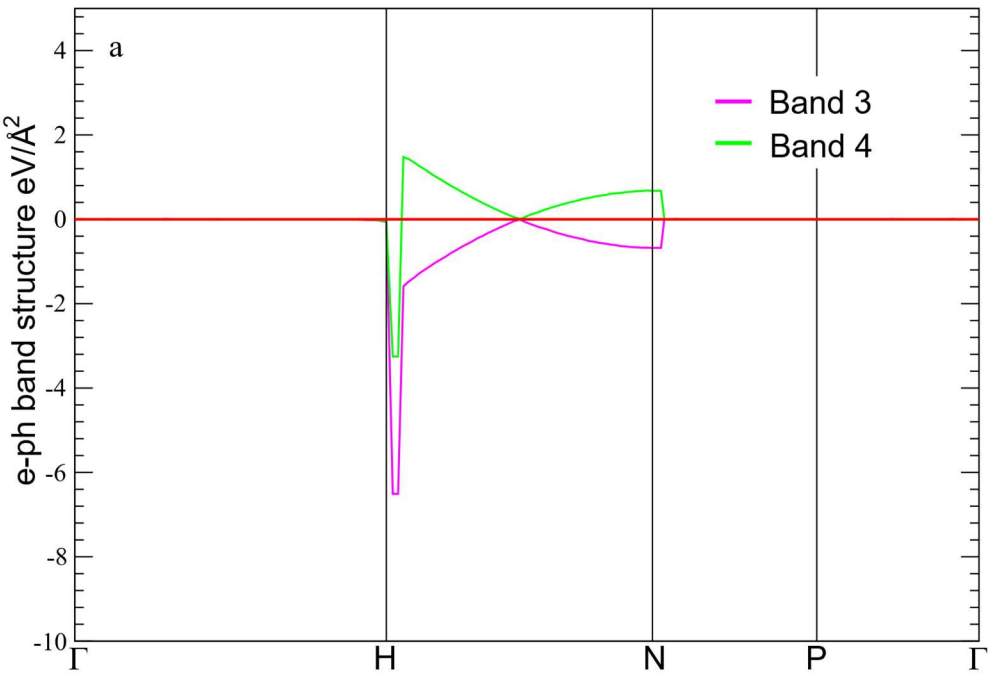

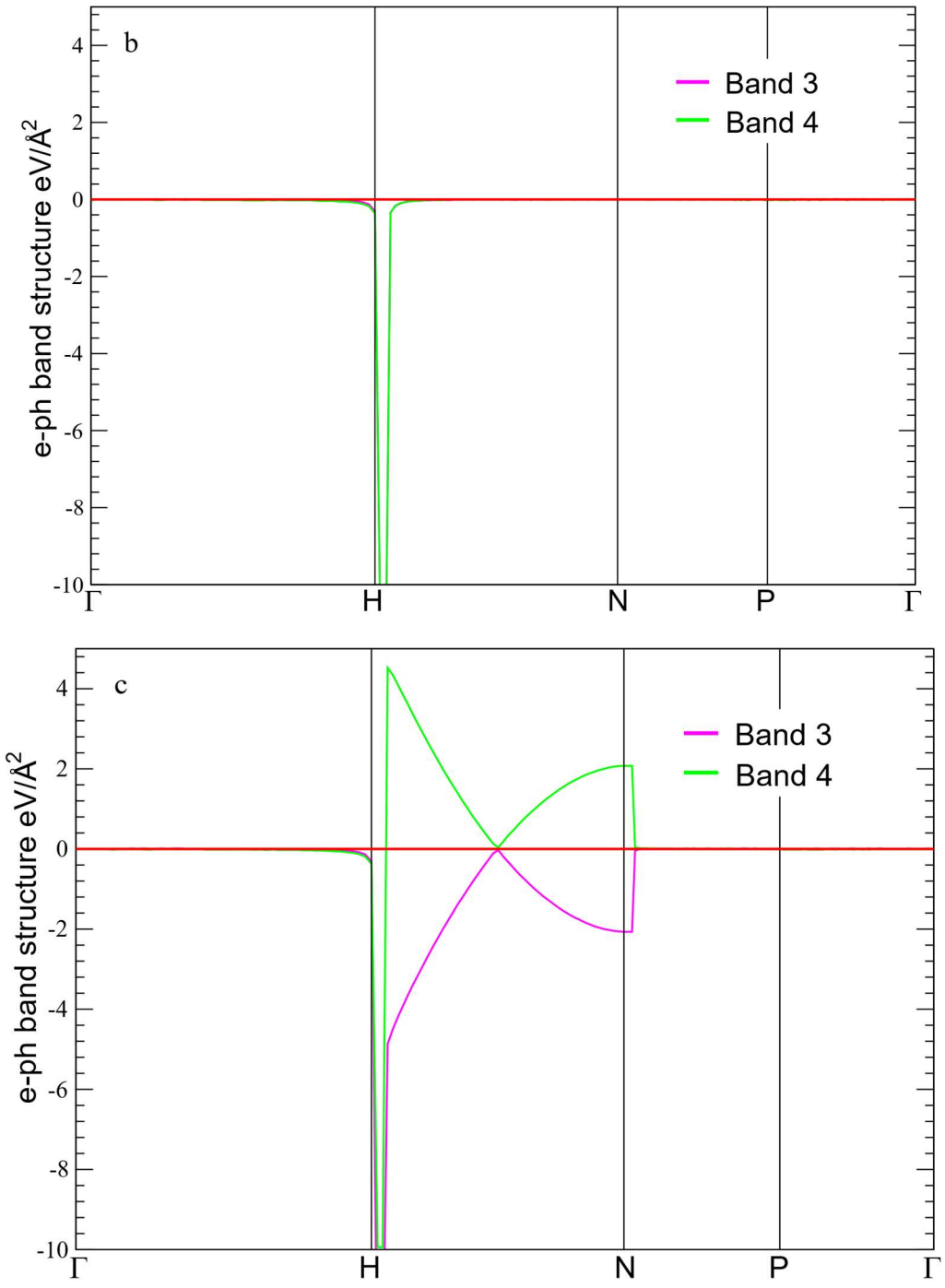

Figure S9. Mode-resolved electron–phonon band structures of lithium, characterized by the second-order derivatives of the band energies with respect to phonon displacements at the H point (q = 0.5, -0.5, 0.5) and plotted along high-symmetry paths in the Brillouin zone (e.g. Γ–H–N–P–Γ).

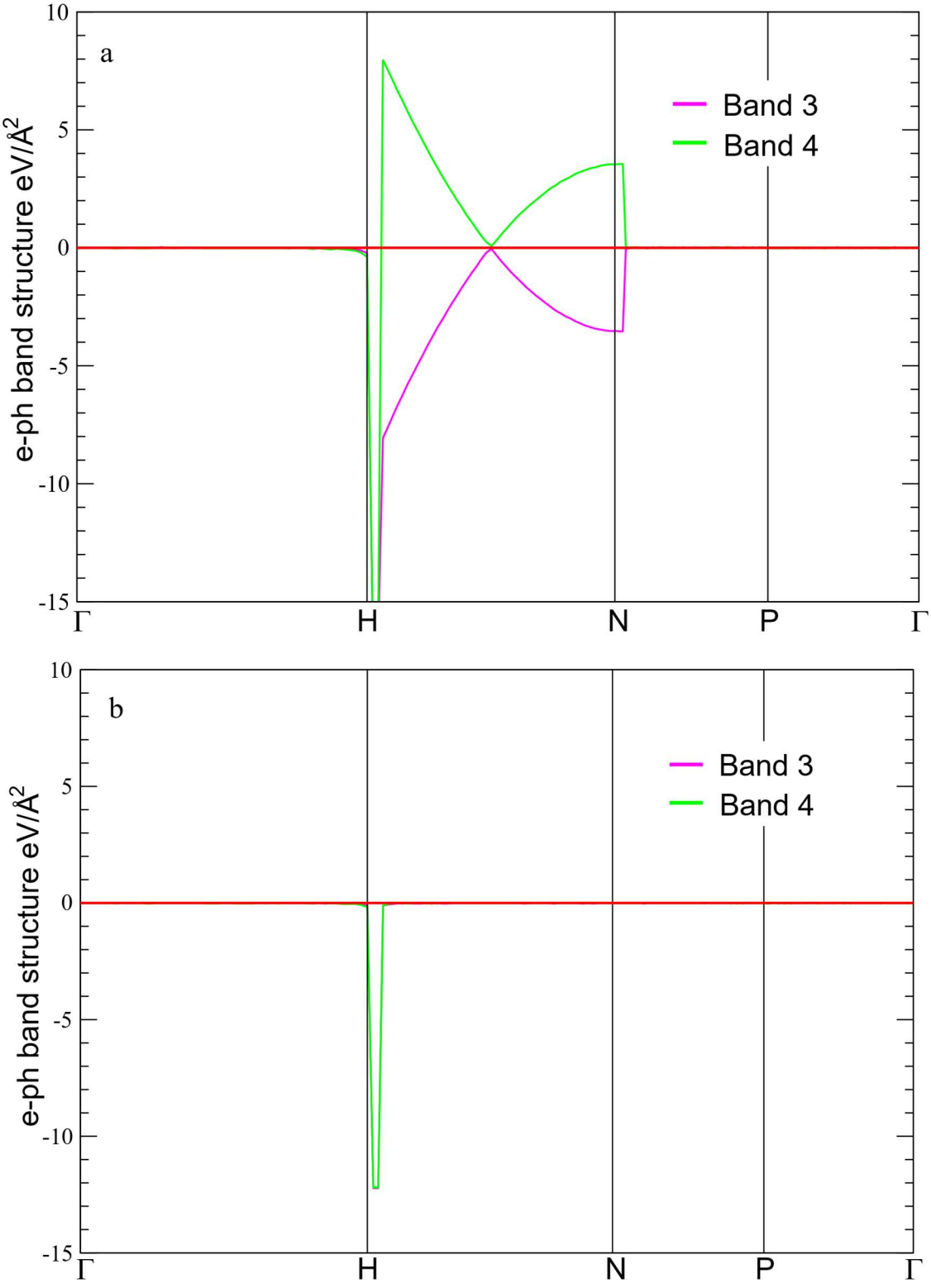
a
b
Band 3
Band 4
e-ph band structure eV/Å^2
10
5
0
-5
-10
-15
Γ
H
N
P
Γ

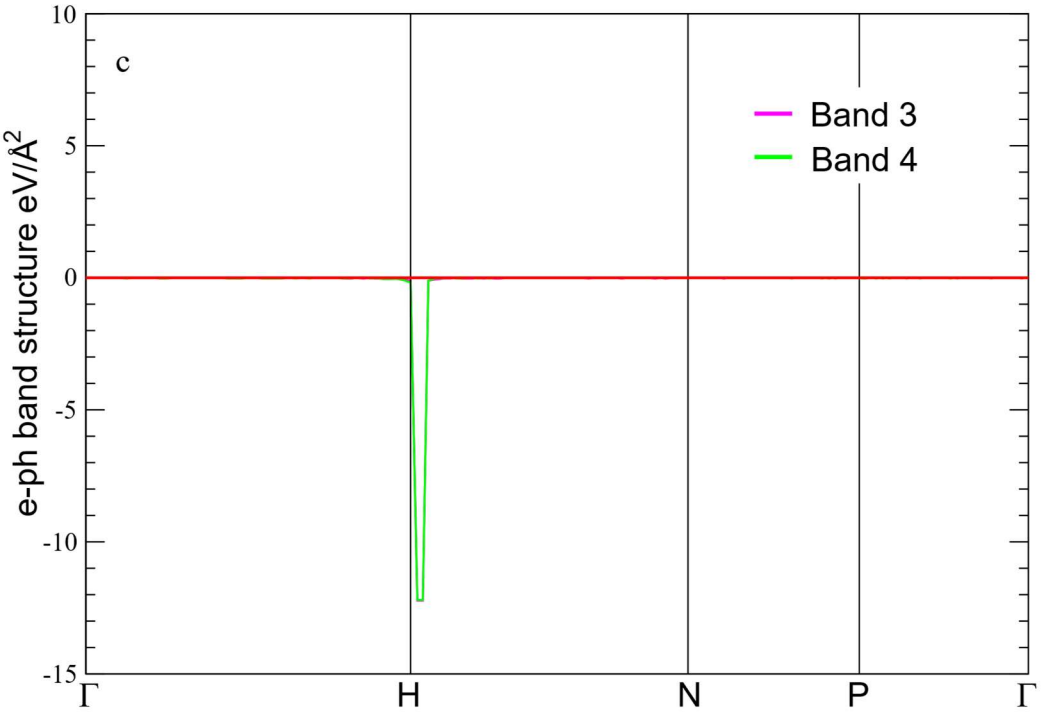

Figure S10. Mode-resolved electron–phonon band structures of lithium, characterized by the second-order derivatives of the band energies with respect to phonon displacements at the N point (q = 0.0, 0.0, 0.5) and plotted along high-symmetry paths in the Brillouin zone (e.g. Γ–H–N–P–Γ).

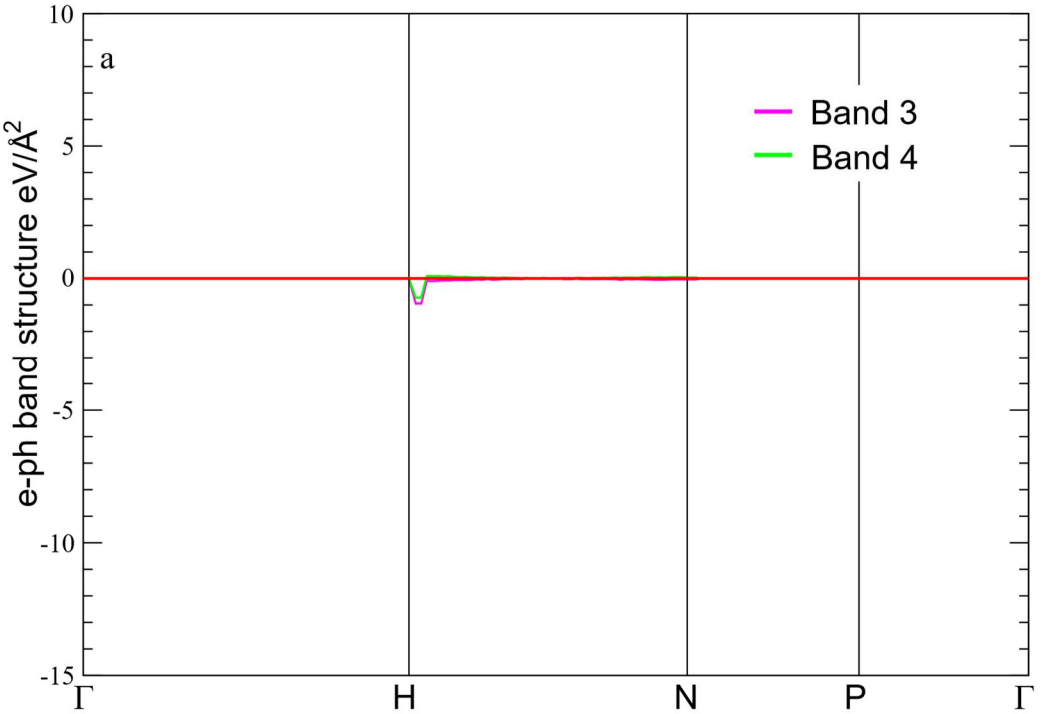

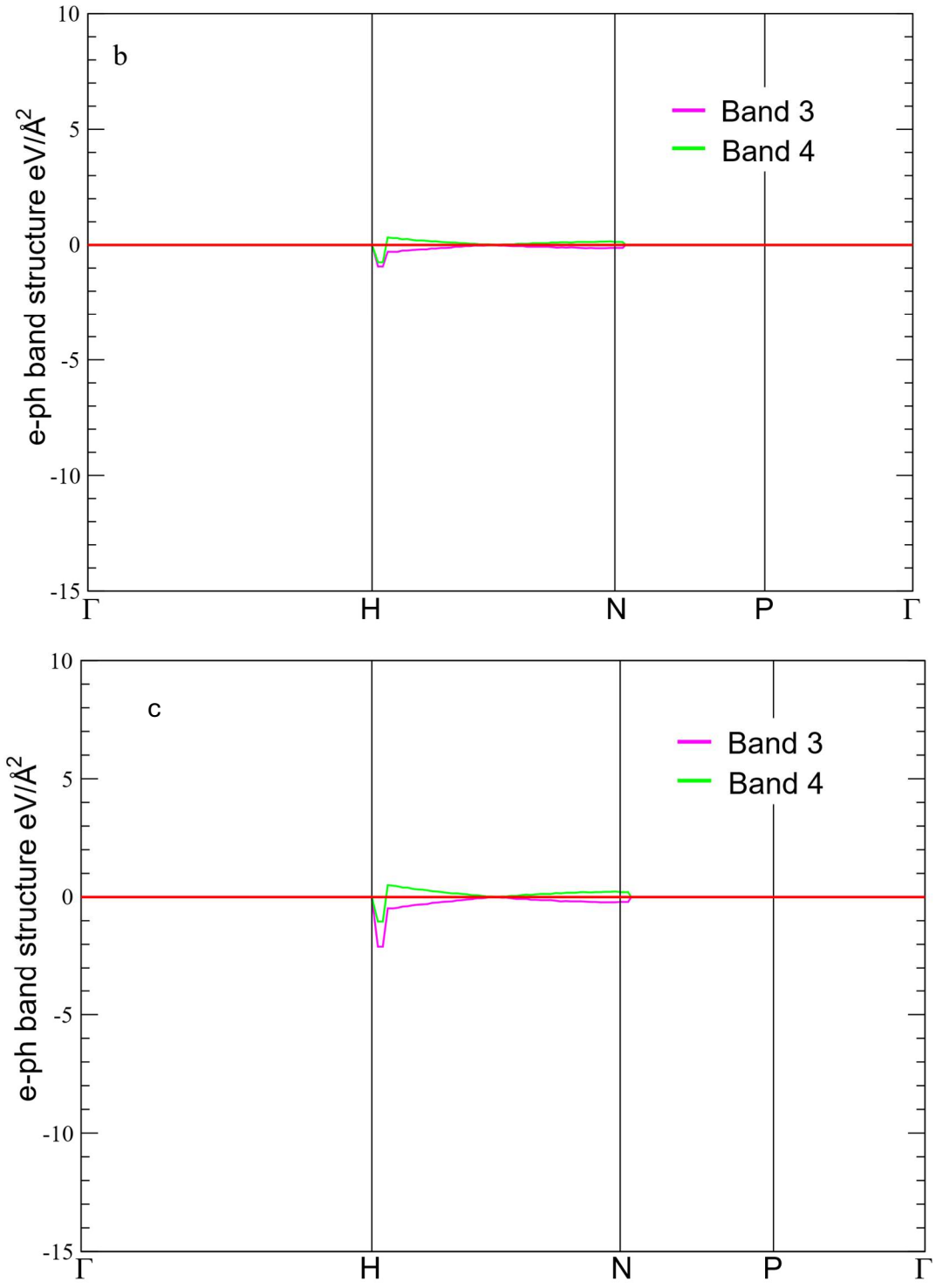

Figure S11. Mode-resolved electron–phonon band structures of lithium, characterized by the second-order derivatives of the band energies with respect to phonon displacements at the P point (q = 0.25, 0.25, 0.25) and plotted along high-symmetry paths in the Brillouin zone (e.g. Γ–H–N–P–Γ).

Dirac cone fitting

Band extraction and fitting.
We first zoom in on a short segment of the mode-resolved electron-phonon band structure path that passes through the suspected crossing. For Li, Rb, and Cs, this is the hourglass-shaped part long the H-N path. Within this small window we treat the two partner branches separately and fit each one with a straight line (Figure S11a). From where the two fitted lines meet, we read off the "Dirac point" in momentum (the crossing location along the path) and in energy. The slopes of the two lines give the speeds of the two branches along that direction in k-space (their directional Fermi velocities).

Local Dirac model and spectral rendering.
To visualize what the dispersion looks like around the crossing, not just along the single path, we build a two-band "Dirac" model in the 2D plane perpendicular to the path. The model uses the fitted velocity to set how steep the cone. Evaluating this model over a grid produces two smooth conical surfaces (upper and lower branches).

Topological diagnostic (local).
On the same grid we compute the Berry curvature of the lower branch from the model and add it up over the plotted region. When the grid extends well beyond the small gap scale, that integral is very close to an integer (about ±1), with the sign set by the sign of the gap. This serves as a compact, local indicator of a chiral source of Berry flux near the crossing. It is a useful mechanistic check that complements but does not replace full Brillouin-zone diagnostics such as Wilson loops or explicit Weyl-charge calculations.

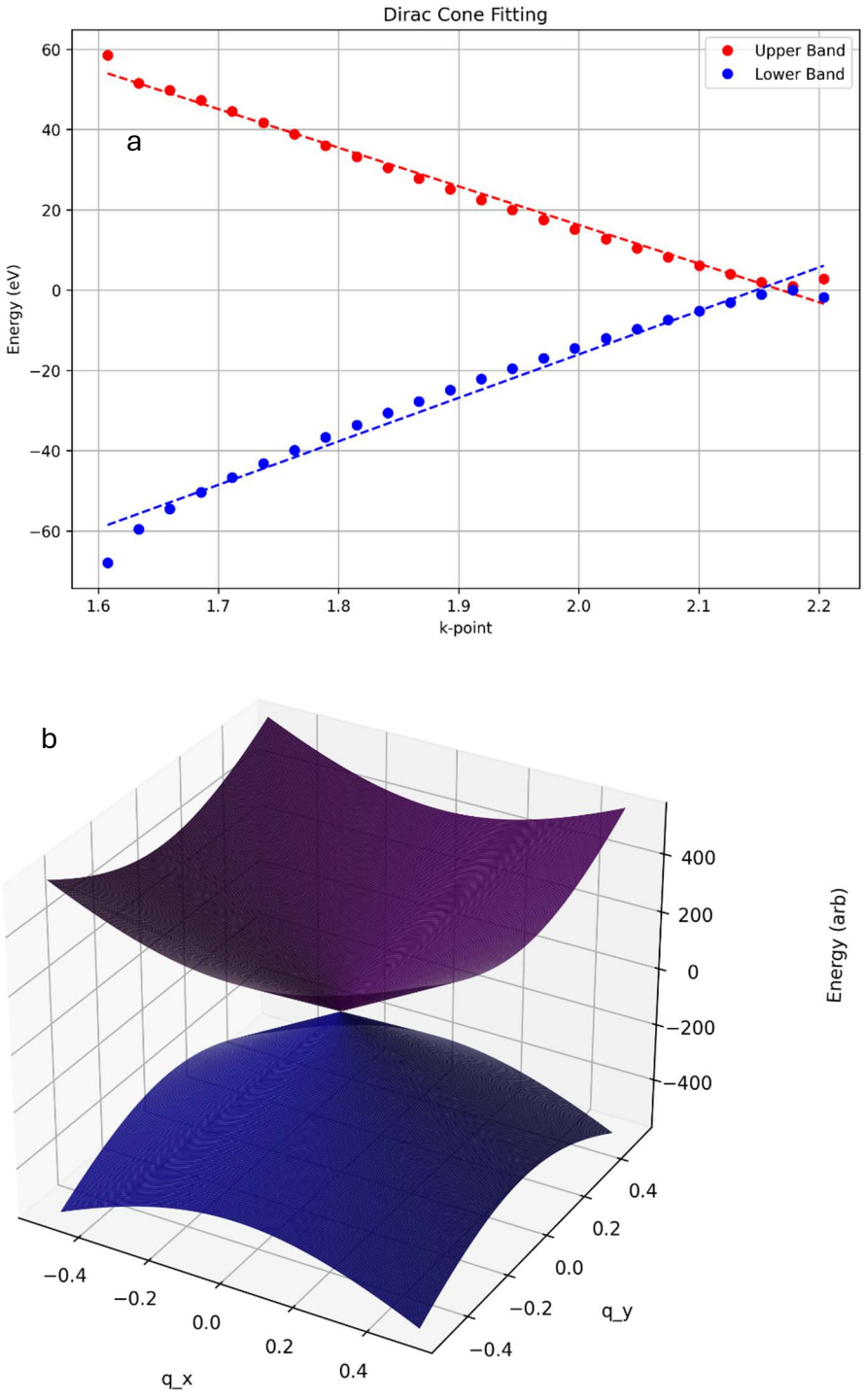

Figure S12. (a) Fitted band data along the selected H-N path for Li. The dots represent the actual data, and the dashed line represents fitted data. This fit provides the parameters used to build the local two-band model. (b) Three-dimensional rendering of the calibrated two-band Dirac Hamiltonian. A small gap rounds the node, producing upper and lower conical sheets; shading reflects a Gaussian spectral weight that emphasizes the near-node region.

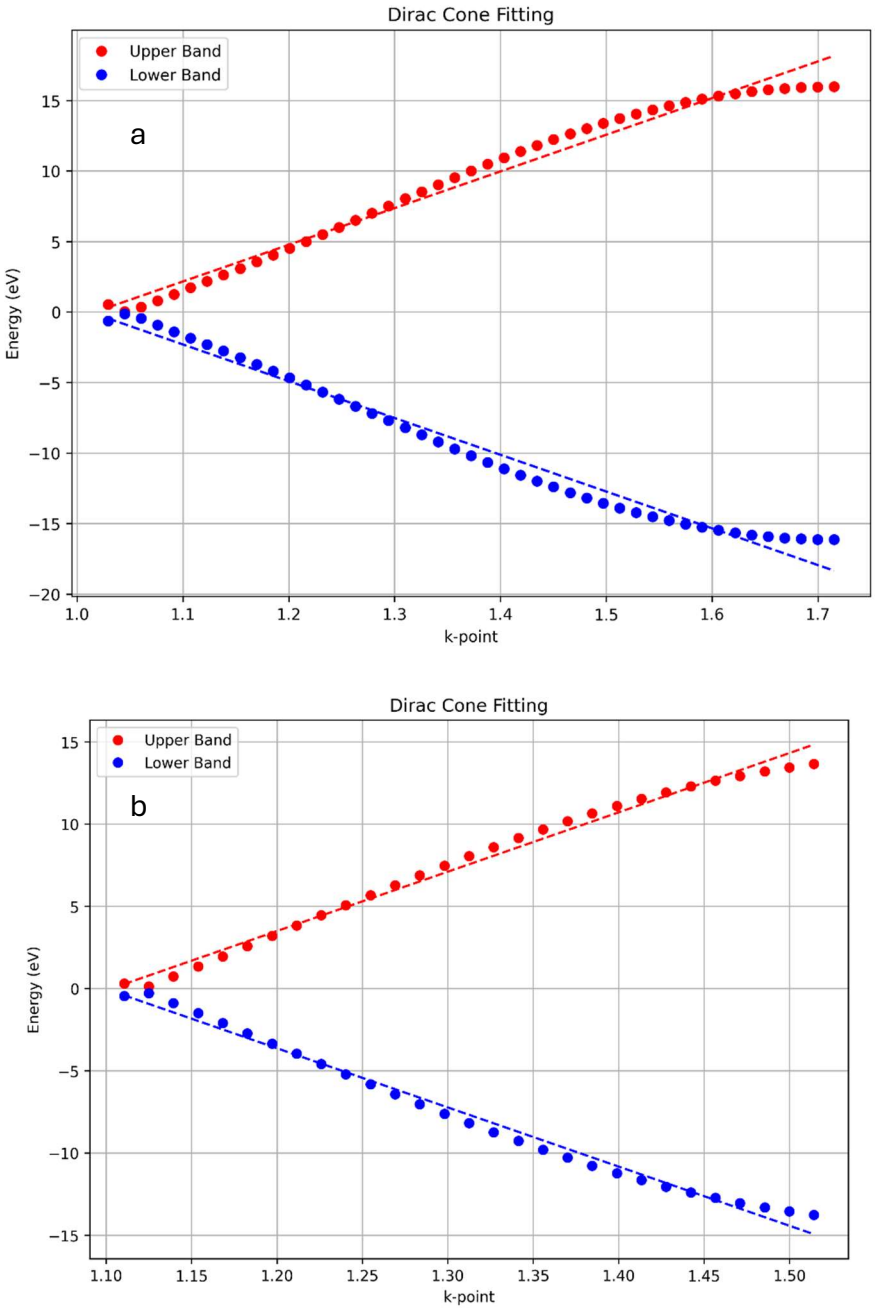

Figure S12. Fitted band data along the selected H-N path for Rb (a) and Cs (b). The dots represent the actual data, and the dashed line represents fitted data. This fit provides the parameters used to build the local two-band model.